Biodistribution, Tumor Detection, and Radiation Dosimetry of ^{18}F-DCFBC, a Low-Molecular-Weight Inhibitor of Prostate-Specific Membrane Antigen, in Patients with Metastatic Prostate Cancer

Steve Y. Cho[1,2], Kenneth L. Gage[1], Ronnie C. Mease[1,2], Srinivasan Senthamizhchelvan[1], Daniel P. Holt[1], Akimosa Jeffrey-Kwanisai[1], Christopher J. Endres[1], Robert F. Dannals[1], George Sgouros[1], Martin Lodge[1], Mario A. Eisenberger[2], Ronald Rodriguez[2,3], Michael A. Carducci[3], Camilo Rojas[4], Barbara S. Slusher[4], Alan P. Kozikowski[5], and Martin G. Pomper[1,2]

[1]Russell H. Morgan Department of Radiology and Radiological Science, Johns Hopkins University, Baltimore, Maryland; [2]Sidney Kimmel Comprehensive Cancer Center, Johns Hopkins University, Baltimore, Maryland; [3]Brady Urological Institute, Johns Hopkins University, Baltimore, Maryland; [4]Brain Sciences Institute of Johns Hopkins University School of Medicine, Johns Hopkins University, Baltimore, Maryland; and [5]Department of Medicinal Chemistry and Pharmacognosy, University of Illinois at Chicago College of Pharmacy, Chicago, Illinois

Prostate-specific membrane antigen (PSMA) is a type II integral membrane protein expressed on the surface of prostate cancer (PCa) cells, particularly in androgen-independent, advanced, and metastatic disease. Previously, we demonstrated that *N*-[*N*-[(*S*)-1,3-dicarboxypropyl]carbamoyl]-4-^{18}F-fluorobenzyl-L-cysteine (^{18}F-DCFBC) could image an experimental model of PSMA-positive PCa using PET. Here, we describe the initial clinical experience and radiation dosimetry of ^{18}F-DCFBC in men with metastatic PCa. **Methods:** Five patients with radiologic evidence of metastatic PCa were studied after the intravenous administration of 370 MBq (10 mCi) of ^{18}F-DCFBC. Serial PET was performed until 2 h after administration. Time–activity curves were generated for selected normal tissues and metastatic foci. Radiation dose estimates were calculated using OLINDA/EXM 1.1. **Results:** Most vascular organs demonstrated a slow decrease in radioactivity concentration over time consistent with clearance from the blood pool, with primarily urinary radiotracer excretion. Thirty-two PET-positive suspected metastatic sites were identified, with 21 concordant on both PET and conventional imaging for abnormal findings compatible with metastatic disease. Of the 11 PET-positive sites not identified on conventional imaging, most were within the bone and could be considered suggestive for the detection of early bone metastases, although further validation is needed. The highest mean absorbed dose per unit administered radioactivity (μGy/MBq) was in the bladder wall (32.4), and the resultant effective dose was 19.9 ± 1.34 μSv/MBq (mean ± SD). **Conclusion:** Although further studies are needed for validation, our findings demonstrate the potential of ^{18}F-DCFBC as a new positron-emitting imaging agent for the detection of metastatic PCa. This study also provides dose estimates for ^{18}F-DCFBC that are comparable to those of other PET radiopharmaceuticals such as ^{18}F-FDG.

Key Words: prostate-specific membrane antigen; prostate cancer; ^{18}F; urea; PET/CT

J Nucl Med 2012; 53:1883–1891
DOI: 10.2967/jnumed.112.104661

Prostate cancer (PCa) is the most commonly diagnosed cancer and the second leading cause of cancer death among men in the United States (*1*). The early detection and improved local therapies for primary PCa have greatly improved survival. However, most patients will still experience relapse and require continued surveillance and ongoing therapy (*2*). In addition to hormonal therapy and antitubulin-based chemotherapy, several promising new targets and therapeutic agents have recently been approved for patients with castrate-resistant PCa (*3*). These recent advances suggest that accurate detection and characterization of disease by molecular imaging will have an increasing impact on clinical management and patient-specific therapeutic optimization.

The prostate-specific membrane antigen (PSMA) is a promising, well-characterized biomarker of PCa and is associated with tumor aggressiveness. Histologic studies have associated high PSMA expression with metastasis (*4*), androgen independence (*5*), and progression (*6*). Previous attempts to image PSMA by SPECT using the agent ^{111}In-capromab pendetide (ProstaScint™; EUSA Pharma), approved by the Food and Drug Administration, demonstrated poor performance due to several factors, including the inherent limitations of intact antibody-mediated imaging (poor tumor penetration and slow blood-pool clearance),

Received Feb. 17, 2012; revision accepted Aug. 6, 2012.
For correspondence or reprints contact: Martin G. Pomper, Johns Hopkins University School of Medicine, 1550 Orleans St., 492 CRB II, Baltimore, MD 21287-0014.
E-mail: mpomper@jhmi.edu

the relatively coarse resolution of SPECT, and the fact that the 7E11-C5.3 antibody on which ^{111}In-capromab pendetide is based binds to an intracellular epitope of PSMA (*7*). New antibody-based PET agents for PSMA are continually emerging and show promise both in preclinical models and in clinical studies (*8,9*). We believe that imaging agents of low molecular weight have inherent advantages over antibodies, such as rapid tumor uptake and clearance from nontarget sites. Many low-molecular-weight inhibitors of PSMA have been reported (*10,11*), and this topic has recently been reviewed (*12*). *N*-[*N*-[(*S*)-1,3-dicarboxypropyl]carbamoyl]-4-fluorobenzyl-L-cysteine (DCFBC) is a low-molecular-weight, urea-based inhibitor of PSMA. We hypothesized that ^{18}F-DCFBC PET/CT may augment molecular imaging of PCa for several reasons. As a druglike molecule, it should have rapid and high tumor penetration along with rapid blood-pool clearance, compared with radiolabeled antibodies, allowing for higher tumor-to-background ratios. It targets a more accessible, external binding domain of PSMA, rather than an intracellular domain. Additionally, PET allows for higher resolution and is highly amenable to quantification, and the relatively long (110 min) physical half-life of ^{18}F enables regional clinical distribution. Here, we report the biodistribution and dosimetry of ^{18}F-DCFBC in patients and a preliminary assessment of ^{18}F-DCFBC in the detection of metastatic PCa.

MATERIALS AND METHODS

Supplemental Materials and Methods as well as Results are available online only at http://jnm.snmjournals.org.

Chemistry

2-[3-(1-Carboxy-2-mercapto-ethyl)-ureido]-pentanedioic acid (compound 1 in Supplemental Fig. 1) was prepared as previously described (*13*). 2-{3-[1-Carboxy-2-(4-fluoro-benzylsulfanyl)-ethyl]-ureido}-pentanedioic acid, or alternatively named *N*-[*N*-[(*S*)-1,3-dicarboxypropyl]carbamoyl]-4-fluorobenzyl-L-cysteine (DCFBC) was prepared according to a modification of a literature procedure to conform to current good manufacturing practice (*11*).

Radiochemistry

2-{3-[1-Carboxy-2-(4-^{18}F-fluoro-benzylsulfanyl)-ethyl]-ureido}-pentanedioic acid, or alternatively named *N*-[*N*-[(*S*)-1,3-dicarboxypropyl]carbamoyl]-4-^{18}F-fluorobenzyl-L-cysteine (^{18}F-DCFBC) (Supplemental Fig. 1) was prepared using an in-house radiochemistry microwave system that allows for remote and semiautomated, complete ^{18}F-fluoride syntheses, including ^{18}F-fluoride trapping and release, ^{18}F-fluoride drying, multistep syntheses, and product reformulation (supplemental data, "Radiochemistry" section) (*14*). For the imaging studies reported here, 4 radiosyntheses were performed, with 1 radiosynthesis supplying enough activity for 2 patients imaged on the same day,—resulting in an average non–decay-corrected yield from ^{18}F-fluoride of 9.25% ± 1.5%, with an average specific activity of 1,190 ± 894 GBq/μmole (32,174 ± 24,169 Ci/mmol) and a radiochemical purity of 97.6% ± 0.6%.

Patient Population and Selection

All studies were performed in accordance with the Johns Hopkins University Institutional Review Board under a Food and Drug Administration exploratory investigational new drug application (eIND 108943). All patients signed an informed consent form. For patients to be included in the study, the following were required: histologic confirmation of PCa; radiologic evidence of new or progressive metastatic disease demonstrated using a conventional imaging modality (CIM), which consisted of bone scintigraphy, CT, ultrasound, or MRI; and a prostate-specific antigen level of 1.0 ng/mL or more. Patients were allowed to be receiving androgen-deprivation therapy if the dose of their medication had been stable for 1 wk or more. Patients underwent monitoring of vital signs at baseline and at intervals after radiopharmaceutical administration (heart rate, respiratory rate, supine blood pressure, and pulse oximetry), electrocardiography, and blood and urine tests (complete blood count with differential, complete metabolic panel, and urinalysis with microscopy) and were queried about concomitant medications and potential adverse events (Common Terminology Criteria for Adverse Events [CTCAE], version 4.0; National Cancer Institute) (*15*).

Five patients with biopsy-proven PCa and radiologic evidence of progressive metastatic disease were enrolled. The median age of the patients was 62 ± 10.3 (mean ± SD) years (age range, 56–80 y). The median serum level of prostate-specific antigen was 10.5 ± 15.7 ng/mL (range, 9.4–46.5 ng/mL). Serum prostate-specific antigen values were obtained within a median of 20 d of the ^{18}F-DCFBC PET/CT study, with a range of 2–61 d. The average original Gleason scores for the patients was 8.2, with a range of 7–9. Four patients had undergone prostatectomy, and 1 had been treated with brachytherapy and external-beam radiation therapy for his primary disease. At the time of enrollment, 2 patients were on stable hormonal therapy, 2 were off therapy because of progressive disease, and 1 was on valproic acid therapy. Valproic acid was allowed because it did not qualify as chemotherapy or hormonal therapy.

PET Protocol

PET/CT scans were acquired on a Discovery DRX PET/CT scanner (GE Healthcare) operating in 3-dimensional mode and using CT for attenuation correction. PET/CT images for clinical assessment were reviewed and analyzed on an AW workstation (GE Healthcare). Patients were scanned supine, starting from the mid thigh and continuing to the vertex of skull, a distance that included approximately 7–9 fields of view (FOV), depending on the patient's height. Preparation included fasting for 4–6 h before injection of ^{18}F-DCFBC, although the effect of a fasting state on ^{18}F-DCFBC tumor uptake has not been established. An initial low-dose CT scan, preceding the serial PET acquisitions, was used for tissue attenuation correction and anatomic correlation. Patients were injected with 370 ± 37 MBq (10 ± 1 mCi) of ^{18}F-DCFBC by a slow intravenous push and a normal-saline flush. Immediately after radiopharmaceutical injection, sequential serial PET images were acquired with varying PET acquisition times per FOV: 1 min/FOV for the first PET scan, 2 min/FOV for the second PET scan, and 4 min/FOV for the third and fourth (PET4) PET scans. Patients were allowed to leave the table to void between the fourth and fifth (PET5) PET scans, as needed. PET5 (4 min per FOV) was obtained after an additional unenhanced CT scan at 2 h after administration of ^{18}F-DCFBC.

Image Analysis

The PET/CT studies were analyzed prospectively by 1 experienced nuclear medicine physician. PET data were iteratively reconstructed using the ordered-subset expectation maximization

method with CT attenuation correction. The PET/CT scan obtained at 2 h after ^{18}F-DCFBC administration (PET5) was used for the assessment of radiopharmaceutical uptake in metastatic disease because this time point demonstrated the highest ratio of tumor activity to background activity based on visual and quantitative assessment. The visual assessment of ^{18}F-DCFBC PET was considered to be positive if there was focal radioactivity above the adjacent background soft tissue or blood pool corresponding to a lymph node (LN) or bone on the correlative unenhanced CT portion of the PET/CT scan. PET quantitative analysis included region-of-interest (ROI) determination of the maximum standardized uptake value based on lean body mass (SUV_{max}) for each site of suspected positive LN or bone metastasis based on visual assessment. Each patient had a reference physiologic liver and blood-pool average SUV based on lean body mass (SUV_{avg}) determined by a 3-cm spheric ROI in the liver and a circular ROI drawn within the walls of the aorta at the aortic arch, respectively.

The correlation of ^{18}F-DCFBC PET/CT with the most recent CIM included clinical reports and CT and bone scintigraphy images. Comparison CT scans of the chest, abdomen, and pelvis were obtained within a median of 42 d (range, 20–69 d) and bone scintigraphy images within a median of 38 d (range, 20–149 d) before the ^{18}F-DCFBC PET/CT.

Metabolite Analysis

In 2 patients, plasma samples taken after PET4 and PET5 were analyzed for metabolites using the column-switching radio–high-performance liquid chromatography method previously reported (*16*), using a Phenomenex Gemini C18 column (250 × 4.6 mm), 30% acetonitrile/70% 0.1 M phosphate buffer, pH 2.4, as a mobile phase at a flow rate of 2 mL/min.

Organ Contouring

Analyze 10.0 (BIR, Mayo Clinic) was used to draw source organ contours on the CT scans with the acquired PET images as a guide. Organ contours from the initial CT scan were assumed to reflect all organ positions in the first 4 PET acquisitions except for the bladder. The second CT scan acquired before the fifth and final PET acquisition was assumed to reflect organ position in the final PET scan.

Contours were drawn for all male source organs used for calculating absorbed doses in OLINDA/EXM 1.1 (Vanderbilt University) except for the thymus, muscle, and bone (Supplemental Fig. 2). The thymus was excluded because it has often involuted completely in older individuals. Bone was excluded because ^{18}F-DCFBC is not a bone-seeking agent, and the marrow distribution in older individuals treated for PCa may not be well reflected by existing models and data (which tend to reflect healthy, younger individuals) (*17–19*). Care was taken to exclude any pathologic uptake from the ROIs.

Dosimetry

The ROIs derived from the CT scan were overlaid onto the PET images to obtain the average activity concentration in each organ (Bq/cm^3) and the organ volumes. The average activity concentration in each organ was multiplied by the volume to generate the total organ activity at each time point, or the time–activity curve. Organ volumes were converted to patient-specific organ masses using standard organ densities from the literature except in the case of the gastrointestinal tract contents (*17,18*), which were determined using the CT-derived average densities in a manner analogous to that used by Senthamizhchelvan et al. (*20*). Patient-specific data used for dosimetry calculations are detailed in Supplemental Table 1.

Decay-corrected source organ radioactivity concentrations at each time point normalized to administered activity were used to generate time–activity curves to evaluate biodistribution. The time-integrated activity for each organ except the urinary bladder was obtained from the non–decay-corrected time–activity curves by a trapezoidal integration method through all measured time points. Beyond the last measured time point, the remaining radioactivity in each organ was conservatively assumed to be removed through physical decay only. The resulting time-integrated activities were then divided by the injected activity to obtain the time-integrated activity coefficients (TIACs) for each organ. To account for differences between the patient-specific organ masses and those of the Cristy–Eckerman phantom used in OLINDA/EXM, the TIACs were weighted by the ratio of the phantom organ mass to the patient-specific organ mass (*21*). The weighted TIACs (in Bq-h/Bq) for each patient were then used in OLINDA/EXM for dose estimates. The application of the gastrointestinal tract model using OLINDA/EXM (*22*) and of red marrow radioactivity and urinary excretion and bladder wall dose methods (*23*) are detailed in the supplemental data.

RESULTS

Adverse Events

Patients did not experience any severe adverse events. There were 3 adverse events that were classified as either unrelated or unlikely to be attributable to the radiopharmaceutical. Two patients experienced grade 3 blood pressure events using the Common Terminology Criteria for Adverse Events (National Cancer Institute) on routine vital sign assessment after administration of the radiopharmaceutical (patient 1 unrelated; patient 2 unlikely), both of which resolved on 7-d follow-up assessment. Several days after administration of the radiopharmaceutical, a third patient experienced lower back pain that began during physical exertion and was considered unrelated to the radiopharmaceutical.

Normal-Organ Biodistribution

The mean organ time–activity curves are shown in Figure 1. In the case of red marrow, ROI volumes were corrected to account for the spongiosa and marrow volume fractions (*18*) and the marrow cellularity (Supplemental Fig. 3) (*24*). The average activity concentration in the bladder is shown to rise throughout the imaging process, compatible with ongoing renal excretion. The biologic excretion half-life through the renal pathway ranged from 11.7 to 26.9 h, with an average of 18.3 ± 7.1 h. Because most patients voided between the fourth and fifth PET scans, the fifth data point represents the sum of the radioactivity within the bladder ROI and the excreted activity.

Tumor Uptake

Thirty-two PET-positive sites were seen in 5 patients, and each patient had at least 3 sites positive for PET by visual assessment. Patient-specific clinical information and imaging findings are detailed in Supplemental Table 2. Two patients had a large number of PET-positive sites, one with 12 PET lesions (11 bone, 1 LN) and the other with 10 PET

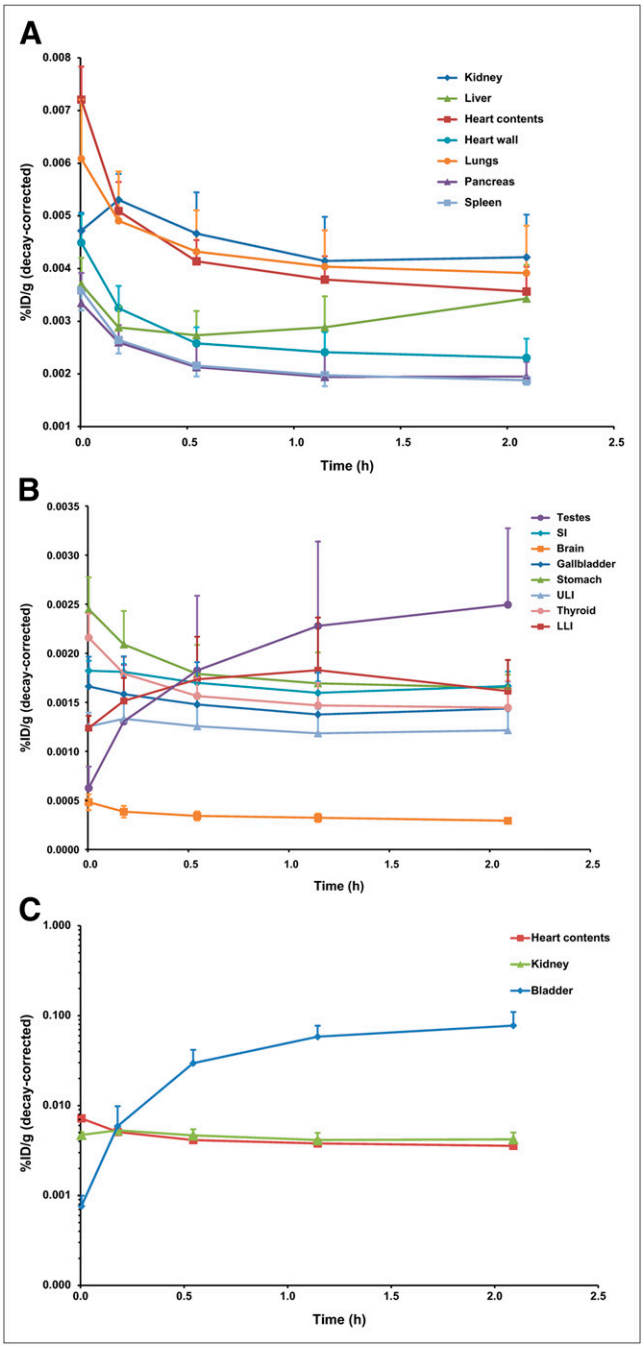

FIGURE 1. Mean biodistribution curves plotted for decay-corrected percentage injected dose per gram of organ mass vs. time. Time axis represents average time over all patients for each PET scan because some patients (i.e., tall patients) required more bed positions. (A) Organs with higher uptake. (B) Organs with lower uptake. (C) Increasing urinary bladder activity. LLI = lower large intestine; SI = small intestine; ULI = upper large intestine. %ID/g = percentage injected dose per gram of organ mass.

lesions (2 bone, 8 LN). Of 32 total PET sites considered positive for metastatic disease, 15 were in the bone and 17 in LNs. The median LN SUV_{max} was 5.6 (range, 2.3–11.6), and the median bone SUV_{max} was 3.6 (range, 2.6–8.2). Examples of PET images are shown in Figure 2. ^{18}F-DCFBC tumor uptake time–activity curves for selected

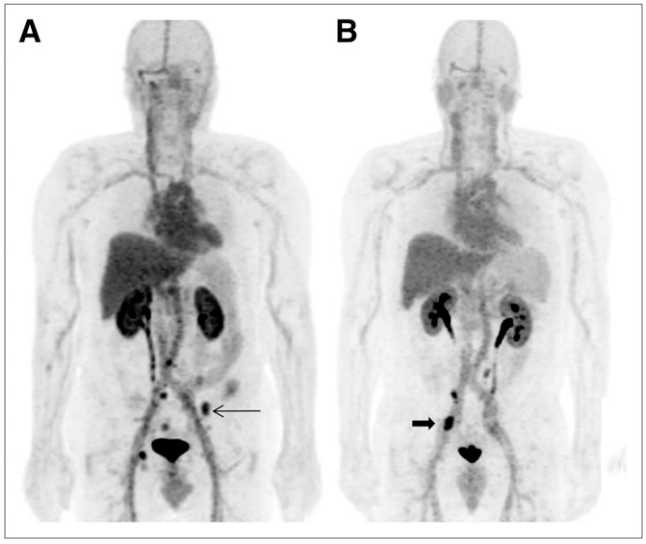

FIGURE 2. ^{18}F-DCFBC PET anterior projection maximal-intensity-projection images at 2 h after injection in patient 1, with several bone metastases (arrow) (A), and patient 5, with LN metastases (arrow) (B), as confirmed by correlation to CT portion of PET/CT exam.

LN and bone sites demonstrated increasing uptake over time relative to the reference blood pool, compatible with tumor-specific uptake (Supplemental Fig. 4).

Forty-two lesions were seen on both PET and CIM. Of a total of 32 PET-positive sites, 21 sites were concordant on both PET and CIM for abnormal findings, compatible with metastatic disease. Five of those 21 concordant sites were in the bone, 3 seen on bone scanning and 2 seen on both bone scanning and CT. The remaining 16 of the 21 concordant sites were seen in the LNs on CT. Examples are given in Figure 3.

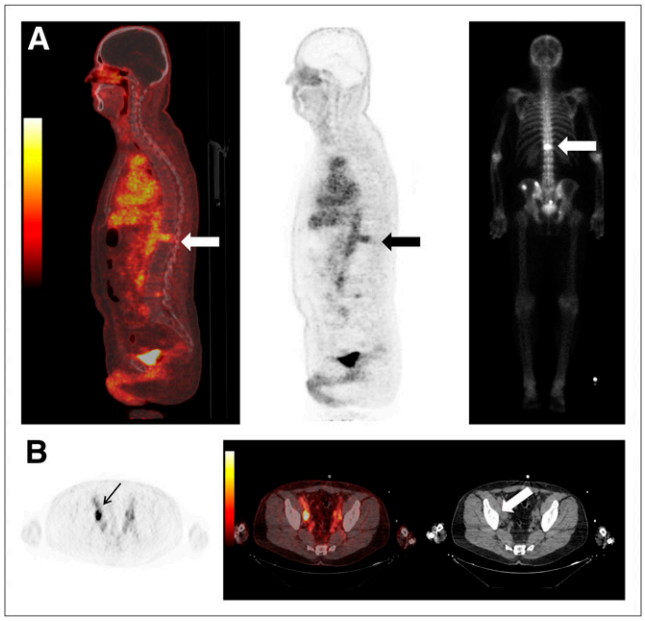

FIGURE 3. Examples of concordant findings on ^{18}F-DCFBC PET and CIM: (A) T12 bone metastasis (arrows) seen on bone scan (far right) and (B) retroperitoneal right external iliac LN (arrow) seen on CT (arrow).

Of PET- and CIM-discordant sites, there were 11 that were PET-positive but CIM-negative and conversely 10 sites that were positive on CIM but negative on PET. The 11 PET-positive sites not detectable by CIM consisted of a subcentimeter LN (Fig. 4) and 10 sites of ^{18}F-DCFBC uptake corresponding to bone on the fused (PET and CT) images that were negative on CT or bone scanning for metastatic disease (Fig. 5). Of the 10 sites that were seen on CT or bone scanning but not on PET, 1 consisted of an enlarging 1.2-cm sclerotic lesion considered suggestive of new bone metastasis (Fig. 6) and 2 smaller, new subcentimeter sclerotic lesions that were nonspecific for benign or malignant etiology. In addition, the remaining 7 sites seen on bone scanning were clinically stable on serial bone scans and considered to be chronic changes or a benign fracture on clinical interpretation.

^{18}F-DCFBC Metabolism

In the 2 patients studied (patients 1 and 2), essentially no metabolism of ^{18}F-DCFBC was observed in plasma after PET4 and PET5. After PET4, 98.3% and 98.2% of the radioactivity eluted with the retention time of intact ^{18}F-DCFBC (8.2 min) for patients 1 and 2, respectively. After PET5, the percentage of the radioactivity eluting at the characteristic time was 95.7% and 97.2% for patients 1 and 2, respectively. The foregoing values are essentially identical and the same as the radiochemical purity measured at the end of synthesis. When blood samples were segregated into cells and plasma, ^{18}F-DCFBC activity was found to a greater extent within the plasma fraction (supplemental data; Supplemental Fig. 5).

Dosimetry

The average TIACs (Bq-h/Bq) for the source organs are shown in Table 1. Individual patient data are provided in Supplemental Table 3. Estimates for the red marrow activity coefficients were obtained using ROIs drawn on both the femoral heads and the spine. The TIAC for red marrow estimated from the femoral head ROI was selected for subsequent dose calculations, because it was larger and would represent a conservative estimate. Determination of the TIAC for the urinary bladder contents required the selection of an appropriate voiding period. Supplemental Figure 6 shows the effect of voiding period on the TIAC for the urinary bladder contents using the dynamic bladder model of Cloutier et al. (*23*). A voiding time of 1 h was selected because patients with treated PCa can have difficulty maintaining continence, and it is expected that patients would void before imaging in general clinical practice.

The average organ-absorbed doses are shown in Table 2. Individual patient data are shown in Supplemental Table 4. The organ with the highest mean absorbed dose (μGy/MBq) is the urinary bladder wall (32.4), followed by the stomach wall (30.2), heart wall (29.2), and kidneys (28.4). The remaining gastrointestinal tract organs (small intestine, upper large intestine, and lower large intestine), liver, and lungs receive lower absorbed doses. The mean effective dose was 19.9 ± 1.34 μSv/MBq.

DISCUSSION

CIMs—that is, bone scintigraphy, CT, ultrasound, and MRI—are currently used to detect primary and metastatic PCa for staging and prognosis or risk stratification (*25*). However, there are inherent limitations to those primarily anatomic techniques. Molecular imaging, such as with a radiopharmaceutical that binds to an informative target, may be able to report on more relevant biochemical features of PCa. For example, knowledge of PSMA expression within

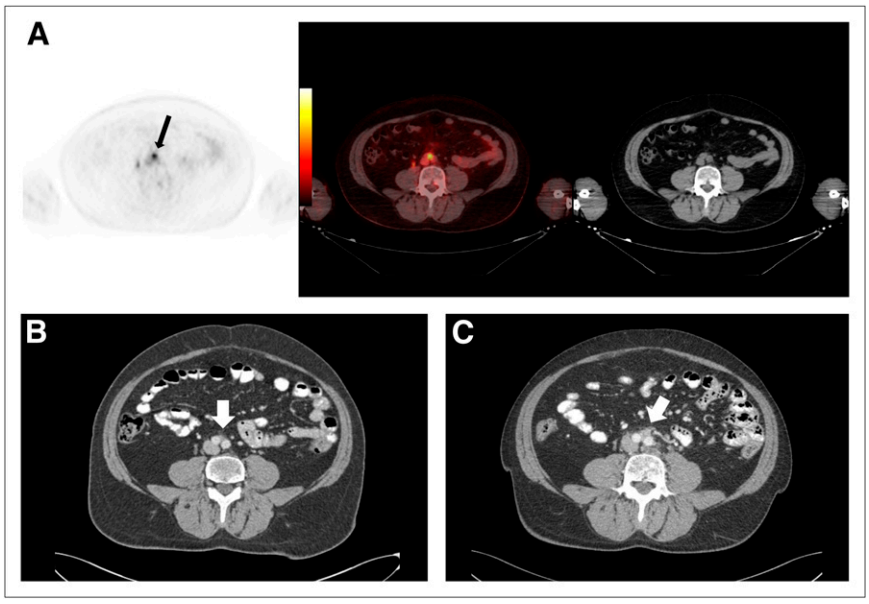

FIGURE 4. (A and B) Focal ^{18}F-DCFBC PET uptake at aortic bifurcation (arrow, A) with correlative small LN seen on concurrent contrast-enhanced CT (arrow, B), not considered to be nodal metastasis by CT but positive by PET. (C) Retrospective review of prior contrast-enhanced CT scan obtained 1 y previously demonstrates LN in this region (arrow).

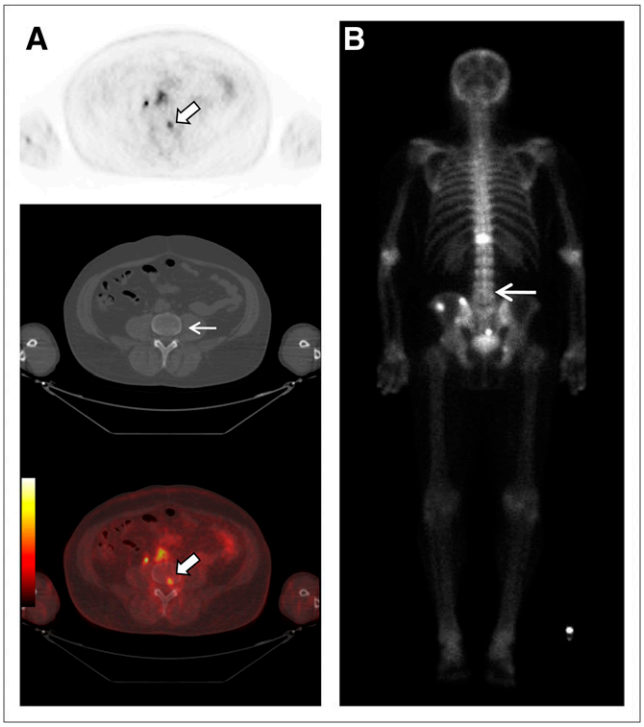

FIGURE 5. Focal ^{18}F-DCFBC PET uptake in L4 vertebral body on PET and fused PET/CT (thick arrows, A) with no correlative abnormality on CT (thin arrow, A) or bone scan (arrow, B).

tumors has been leveraged to provide information about prognosis (*6*), response to chemotherapy (*26*), and androgen signaling (*27*) through imaging. Distinguishing lethal from nonlethal disease is an overarching challenge for the imaging of PCa (*25*).

One current PET radiopharmaceutical for PCa is ^{18}F-FDG, which is not sufficiently sensitive for diagnosis, although several studies have demonstrated the utility of ^{18}F-FDG as a biomarker of progression in advanced PCa (*28*). Other radiopharmaceuticals, with higher PCa uptake than ^{18}F-FDG, include ^{11}C-choline, ^{18}F-fluorocholine, and ^{11}C-acetate. Those compounds have been extensively studied in a variety of clinical scenarios but have yielded mixed results. One problem is that they all demonstrate a certain degree of overlap in terms of lesion uptake between PCa and benign inflammatory processes (*29,30*). ^{18}F-Fluoride PET for identifying bone metastases has proven sensitive but is unable to differentiate between viable tumor and chronic reactive bone changes (*31*). Other promising radiopharmaceuticals for PCa include anti-1-amino-3-^{18}F-fluorocyclobutane-1-carboxylic acid and ^{18}F-fluorodihydrotestosterone, which are also actively undergoing clinical evaluation in a variety of settings (*32,33*). The first urea-based PSMA-targeting radiopharmaceutical to undergo clinical testing is Trofex™ (^{123}I-MIP 1072 and ^{123}I-MIP 1095; Molecular Insight Pharmaceuticals, Inc.), which has been used to good advantage in detecting metastatic disease with SPECT (*34*). ^{18}F-DCFBC is structurally similar and represents one of several radiolabeled, urea-based inhibitors of PSMA that have been synthesized and tested as PET agents for PCa (*12*).

In this study, ^{18}F-DCFBC PET/CT was performed in 5 patients with PCa who had radiologic evidence of new or progressive metastatic disease with no severe adverse events. Chromatography on patient plasma showed essentially no metabolism or defluorination, with blood radioactivity almost entirely within the plasma component. The clearance of ^{18}F-DCFBC was predominantly by urinary excretion, with radiopharmaceutical accumulation in the urinary bladder and specific, PSMA-mediated uptake in the renal parenchyma, which is a known site of PSMA expression (*35*). There was decreasing but moderately persistent blood-pool and liver activity. The slow rise in decay-corrected hepatic uptake (Fig. 1A) suggests the possibility of some hepatic excretion of ^{18}F-DCFBC with a long biologic elimination period, because the liver does not appear to express PSMA to a significant extent (*35*). The absence of gallbladder filling or intraluminal gastrointestinal tract radioactivity during the scan period indicates that the hepatic elimination period, if it exists, is long enough to be discounted for a radionuclide as short-lived as ^{18}F. As shown in Supplemental Figure 3, ^{18}F-DCFBC appeared to clear more slowly from femoral head marrow than from marrow in the spine, which generally followed the trend of the heart contents. The cause of this difference is unclear but could reflect artifacts from patient motion and changes in positioning during the scan period. The brain demonstrated little uptake, consistent with ^{18}F-DCFBC's hydrophilic nature, which prevented it from crossing an intact blood–brain barrier (*11*).

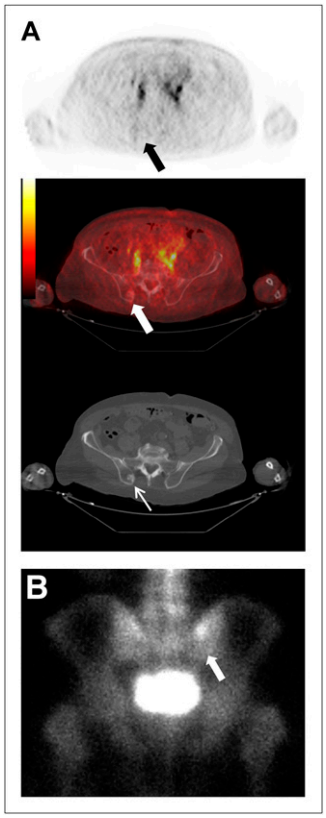

FIGURE 6. (A) New sclerotic lesion in right posterior iliac bone seen on CT (thin white arrow) but not on ^{18}F-DCFBC PET (black arrow) or PET/CT (thick white arrow). (B) Corresponding asymmetric uptake on bone scan (arrow).

TABLE 1
Average TIACs (Bq-h/Bq)

Organ	Average	SD	Percentage coefficient of variation
Adrenals	9.26E−04	2.35E−04	25.43
Brain	1.20E−02	1.30E−03	10.78
Gallbladder contents	2.50E−03	6.87E−04	27.47
Lower large intestine contents	1.40E−02	3.96E−03	28.29
Small intestine contents	4.93E−02	5.35E−03	10.85
Stomach	1.96E−02	3.06E−03	15.55
Upper large intestine contents	1.52E−02	2.55E−03	16.76
Heart contents	4.78E−02	7.26E−03	15.20
Heart wall	2.10E−02	2.58E−03	12.31
Kidneys	3.50E−02	5.84E−03	16.68
Liver	1.59E−01	3.29E−02	20.62
Lungs	1.09E−01	1.87E−02	17.13
Pancreas	5.34E−03	8.93E−04	16.73
Spleen	1.01E−02	8.92E−04	8.80
Testes	2.42E−03	1.00E−03	41.50
Thyroid	8.00E−04	8.23E−05	10.29
Bladder contents	1.26E−01	4.94E−02	39.13
Red marrow (femoral head)	1.08E−01	1.06E−02	9.86
Red marrow (spine)	6.92E−02	7.70E−03	11.12
Total body	2.37E+00	9.09E−02	3.83
Remainder of body	1.72E+00	1.01E−01	5.86

Visual assessment of ^{18}F-DCFBC, in comparison to CIM, demonstrated that most PET-positive sites were concordant with CIM that was indicative of metastatic disease; most of these sites corresponded to LNs on CT. Some of these LNs were small and not definitive for metastatic disease by CT size criteria but were suspected of being early nodal metastases. Nevertheless, because biopsies were not obtained, false-positive ^{18}F-DCFBC uptake is possible. The

TABLE 2
Average Organ-Absorbed Dose (mGy/MBq) and Estimated Effective Dose (mSv/MBq)

Organ	Average	SD	Percentage coefficient of variation
Adrenals	1.85E−02	2.83E−03	15.32
Brain	4.21E−03	2.83E−04	6.73
Breasts	8.51E−03	3.22E−04	3.78
Gallbladder wall	1.79E−02	1.95E−03	10.90
Lower large intestine wall	2.47E−02	3.69E−03	14.92
Small intestine wall	2.36E−02	1.72E−03	7.31
Stomach wall	3.02E−02	3.24E−03	10.72
Upper large intestine wall	2.34E−02	2.20E−03	9.39
Heart wall	2.92E−02	3.24E−03	11.12
Kidneys	2.84E−02	3.81E−03	13.45
Liver	2.46E−02	4.16E−03	16.88
Lungs	2.45E−02	2.99E−03	12.22
Muscle	9.69E−03	3.97E−04	4.10
Ovaries	1.32E−02	5.26E−04	3.99
Pancreas	1.92E−02	2.15E−03	11.19
Red marrow	1.70E−02	9.81E−04	5.79
Osteogenic cells	1.82E−02	8.92E−04	4.90
Skin	7.30E−03	3.50E−04	4.79
Spleen	1.72E−02	1.05E−03	6.08
Testes	1.54E−02	4.19E−03	27.23
Thymus	1.10E−02	4.53E−04	4.12
Thyroid	1.17E−02	6.87E−04	5.88
Bladder wall	3.24E−02	7.24E−03	22.35
Uterus	1.34E−02	2.95E−04	2.20
Total body	1.09E−02	4.28E−04	3.91
Effective dose	1.99E−02	1.34E−03	6.73

moderate degree of persistent blood-pool radioactivity could represent a limitation for the detection of LN metastases adjacent to major vessels by ^{18}F-DCFBC; however, anatomic correlation of the PET scans with CT images should allow unambiguous detection of uptake at these sites.

Sites of discordance between ^{18}F-DCFBC PET and CIM that were PET-positive but CIM-negative were almost all within bone, with no evidence of osseous metastatic disease by CT or bone scanning. However, the bone scans were obtained with whole-body planar imaging, which can have limited detectability, compared with SPECT/CT (*36*) or ^{18}F-NaF PET (*37*) imaging. Whether those sites of discordance represent early bone metastases or false-positives also needs further evaluation in larger studies including correlation with ^{99m}Tc-MDP bone SPECT/CT or ^{18}F-NaF bone PET, biopsy-based histologic confirmation, or long-term clinical follow-up. There were 10 discordant sites that were ^{18}F-DCFBC PET–negative but CIM-positive. One of these sites was an enlarging 1.2-cm sclerotic lesion in the right posterior iliac bone suspected of being a metastasis in a patient who recently began treatment with an oral, nonsteroidal antiandrogen agent 16 d before ^{18}F-DCFBC PET/CT. PSMA expression has been demonstrated to be diminished at the start of antiandrogen therapy (*5*), possibly affecting the sensitivity of the PSMA-based PET detection of metastases in this clinical scenario, but requires further verification in future studies. The remainder of the 9 PET-negative and CIM-positive sites consisted of 2 small sclerotic lesions that were visible on CT but negative on bone scans and indeterminate for bone islands or metastases and 7 other sites of discordant uptake that were positive but stable on serial bone scans and clinically interpreted as representing either chronic changes due to remodeling or benign fracture. However, the true negative predictive value of ^{18}F-DCFBC PET at sites positive on bone scans as representing truly negative sites of metastatic bone disease, allowing for differentiation between metastases and sites of treated disease, requires further study.

We attempted to determine why there was relatively persistent blood-pool radioactivity for this low-molecular-weight agent. To determine whether DCFBC could bind to a circulating form of PSMA that may be present in human blood, which might account for persistent blood-pool radioactivity, we tested the inhibitory capacity of DCFBC in a sample of normal human plasma (*38*). Unlabeled DCFBC bound to the circulating form of PSMA in normal human serum and inhibited its ability to hydrolyze *N*-acetylated aspartyl-glutamate with an inhibitory concentration of 50% of 3 nM (Supplemental Fig. 7). Persistence in the blood pool could also be due to an as-yet-unknown property specific to ^{18}F-DCFBC that requires further investigation.

Despite persistence in the blood pool, the organ and effective dose estimates for ^{18}F-DCFBC compare favorably to ^{18}F-FDG, as shown in Supplemental Figure 8 (*39*), with the overall effective dose for ^{18}F-DCFBC averaging 1.99×10^{-2} mSv/MBq per administered dose (vs. ^{18}F-FDG, estimated at 1.90×10^{-2} mSv/MBq) (*39*). The ^{18}F-DCFBC radiation doses to patients are thus comparable to those of other PET radiopharmaceuticals such as ^{18}F-FDG.

A limitation of this initial study includes the small number of patients studied ($n = 5$) and a heterogeneous population representing metastatic disease at different stages. The scope of this study allowed a comparison of ^{18}F-DCFBC PET to CIM on only a lesion-to-lesion basis, without histologic confirmation of metastatic disease or long-term clinical follow-up to determine the true nature of some of the detected sites. This study merely confirms that ^{18}F-DCFBC PET uptake at multiple sites was concordant with CIM. However, sensitivity and specificity for the detection of metastases by ^{18}F-DCFBC will be answered only through larger, prospective, and more clinically focused imaging trials.

CONCLUSION

This first-in-human clinical study demonstrates the feasibility and potential of using ^{18}F-DCFBC, a low-molecular-weight PSMA-targeted PET radiopharmaceutical, for the detection of metastatic PCa. The estimated ^{18}F-DCFBC radiation doses to patients are consistent with those of other PET radiopharmaceuticals, with a mean effective dose comparable to that of ^{18}F-FDG.

DISCLOSURE STATEMENT

The costs of publication of this article were defrayed in part by the payment of page charges. Therefore, and solely to indicate this fact, this article is hereby marked "advertisement" in accordance with 18 USC section 1734.

ACKNOWLEDGMENTS

We are grateful for the following sources of support: the Prostate Cancer Foundation Young Investigator Award (SYC), RSNA Research and Education Foundation Research Scholar Award (SYC), the Patrick C. Walsh Foundation, NIH NIBIB award T32 EB006351 and NCI CA134675. No other potential conflict of interest relevant to this article was reported.

REFERENCES

1. Jemal A, Siegel R, Xu J, Ward E. Cancer statistics, 2010. *CA Cancer J Clin.* 2010;60:277–300.
2. Walczak JR, Carducci MA. Prostate cancer: a practical approach to current management of recurrent disease. *Mayo Clin Proc.* 2007;82:243–249.
3. Beltran H, Beer TM, Carducci MA, et al. New therapies for castration-resistant prostate cancer: efficacy and safety. *Eur Urol.* 2011;60:279–290.
4. Chang SS, Reuter VE, Heston WD, Gaudin PB. Metastatic renal cell carcinoma neovasculature expresses prostate-specific membrane antigen. *Urology.* 2001;57:801–805.
5. Wright GL Jr, Grob BM, Haley C, et al. Upregulation of prostate-specific membrane antigen after androgen-deprivation therapy. *Urology.* 1996;48:326–334.
6. Perner S, Hofer MD, Kim R, et al. Prostate-specific membrane antigen expression as a predictor of prostate cancer progression. *Hum Pathol.* 2007;38:696–701.
7. Wilkinson S, Chodak G. The role of 111indium-capromab pendetide imaging for assessing biochemical failure after radical prostatectomy. *J Urol.* 2004;172:133–136.
8. Elsässer-Beile U, Reischl G, Wiehr S, et al. PET imaging of prostate cancer xenografts with a highly specific antibody against the prostate-specific membrane antigen. *J Nucl Med.* 2009;50:606–611.

9. Tagawa ST, Beltran H, Vallabhajosula S, et al. Anti-prostate-specific membrane antigen-based radioimmunotherapy for prostate cancer. *Cancer.* 2010;116:1075–1083.
10. Barinka C, Rovenska M, Mlcochova P, et al. Structural insight into the pharmacophore pocket of human glutamate carboxypeptidase II. *J Med Chem.* 2007;50:3267–3273.
11. Mease RC, Dusich CL, Foss CA, et al. N-[N-[(S)-1,3-dicarboxypropyl] carbamoyl]-4-[^{18}F]fluorobenzyl-L-cysteine, [^{18}F]DCFBC: a new imaging probe for prostate cancer. *Clin Cancer Res.* 2008;14:3036–3043.
12. Foss CA, Mease RC, Cho SY, Kim HJ, Pomper MG. GCPII imaging and cancer. *Curr Med Chem.* 2012;19:1346–1359.
13. Kozikowski AP, Nan F, Conti P, et al. Design of remarkably simple, yet potent urea-based inhibitors of glutamate carboxypeptidase II (NAALADase). *J Med Chem.* 2001;44:298–301.
14. Holt DP, Ravert HT, Mathews WB, Horti A, Mease R, Dannals RF. A semi-automated microwave chemistry system for complete radiosynthesis, purification, and formulation of F-18 radiotracers [abstract]. *J Labelled Comp Radiopharm.* 2011;54:S426.
15. Common Terminology Criteria for Adverse Events v.4.0 (CTCAE). National Cancer Institute. Available at: http://ctep.cancer.gov/protocolDevelopment/electronic_applications/ctc.htm. Accessed October 23, 2012.
16. Hilton J, Yokoi F, Dannals RF, Ravert HT, Szabo Z, Wong DF. Column-switching HPLC for the analysis of plasma in PET imaging studies. *Nucl Med Biol.* 2000;27:627–630.
17. International Commission on Radiation Units and Measurements. *Tissue Substitutes in Radiation Dosimetry and Measurement.* Bethesda, MD: International Commission on Radiation Units and Measurements; 1989.
18. Pichardo JC, Trindade AA, Brindle JM, Bolch WE. Method for estimating skeletal spongiosa volume and active marrow mass in the adult male and adult female. *J Nucl Med.* 2007;48:1880–1888.
19. Valentin J. Basic anatomical and physiological data for use in radiological protection: reference values—a report of age- and gender-related differences in the anatomical and physiological characteristics of reference individuals. ICRP Publication 89. International Commission on Radiological Protection; 2002. Available at: http://altmine.mie.uc.edu/nuclear/hplib/icrp/icrp%2089.pdf. Accessed October 23, 2012.
20. Senthamizhchelvan S, Bravo PE, Esaias C, et al. Human biodistribution and radiation dosimetry of ^{82}Rb. *J Nucl Med.* 2010;51:1592–1599.
21. Stabin MG, Siegel JA. Physical models and dose factors for use in internal dose assessment. *Health Phys.* 2003;85:294–310.
22. Stabin M. *Fundamentals of Nuclear Medicine Dosimetry.* New York, NY: Springer; 2008.
23. Cloutier RJ, Smith SA, Watson EE, Snyder WS, Warner GG. Dose to the fetus from radionuclides in the bladder. *Health Phys.* 1973;25:147–161.
24. Leggett RW. Basic anatomical and physiological data for use in radiological protection: the skeleton—a report of a Task Group of Committee 2 of the International Commission on Radiological Protection. *Ann ICRP.* 1995;25:1–80.
25. Kelloff GJ, Choyke P, Coffey DS. Challenges in clinical prostate cancer: role of imaging. *AJR.* 2009;192:1455–1470.
26. Hillier SM, Kern AM, Maresca KP, et al. ^{123}I-MIP-1072, a small-molecule inhibitor of prostate-specific membrane antigen, is effective at monitoring tumor response to taxane therapy. *J Nucl Med.* 2011;52:1087–1093.
27. Evans MJ, Smith-Jones PM, Wongvipat J, et al. Noninvasive measurement of androgen receptor signaling with a positron-emitting radiopharmaceutical that targets prostate-specific membrane antigen. *Proc Natl Acad Sci USA.* 2011; 108:9578–9582.
28. Morris MJ, Akhurst T, Larson SM, et al. Fluorodeoxyglucose positron emission tomography as an outcome measure for castrate metastatic prostate cancer treated with antimicrotubule chemotherapy. *Clin Cancer Res.* 2005;11:3210–3216.
29. Bauman G, Belhocine T, Kovacs M, Ward A, Beheshti M, Rachinsky I. ^{18}F-fluorocholine for prostate cancer imaging: a systematic review of the literature. *Prostate Cancer Prostatic Dis.* 2012;15:45–55.
30. Souvatzoglou M, Weirich G, Schwarzenboeck S, et al. The sensitivity of [^{11}C] choline PET/CT to localize prostate cancer depends on the tumor configuration. *Clin Cancer Res.* 2011;17:3751–3759.
31. Grant FD, Fahey FH, Packard AB, Davis RT, Alavi A, Treves ST. Skeletal PET with ^{18}F-fluoride: applying new technology to an old tracer. *J Nucl Med.* 2008;49:68–78.
32. Beattie BJ, Smith-Jones PM, Jhanwar YS, et al. Pharmacokinetic assessment of the uptake of 16beta-^{18}F-fluoro-5alpha-dihydrotestosterone (FDHT) in prostate tumors as measured by PET. *J Nucl Med.* 2010;51:183–192.
33. Schuster DM, Votaw JR, Nieh PT, et al. Initial experience with the radiotracer anti-1-amino-3-^{18}F-fluorocyclobutane-1-carboxylic acid with PET/CT in prostate carcinoma. *J Nucl Med.* 2007;48:56–63.
34. Barrett JA, LaFrance N, Coleman RE, et al. Targeting metastatic prostate cancer [PCa] in patients with ^{123}I-MIP1072 and ^{123}I-MIP1095 [abstract]. *J Nucl Med.* 2009;50(suppl 2):522.
35. Kinoshita Y, Kuratsukuri K, Landas S, et al. Expression of prostate-specific membrane antigen in normal and malignant human tissues. *World J Surg.* 2006; 30:628–636.
36. Helyar V, Mohan HK, Barwick T, et al. The added value of multislice SPECT/CT in patients with equivocal bony metastasis from carcinoma of the prostate. *Eur J Nucl Med Mol Imaging.* 2010;37:706–713.
37. Even-Sapir E, Metser U, Mishani E, Lievshitz G, Lerman H, Leibovitch I. The detection of bone metastases in patients with high-risk prostate cancer: ^{99m}Tc-MDP Planar bone scintigraphy, single- and multi-field-of-view SPECT, ^{18}F-fluoride PET, and ^{18}F-fluoride PET/CT. *J Nucl Med.* 2006;47:287–297.
38. Rojas C, Frazier ST, Flanary J, Slusher BS. Kinetics and inhibition of glutamate carboxypeptidase II using a microplate assay. *Anal Biochem.* 2002; 310:50–54.
39. International Commission on Radiological Protection. Radiation dose to patients from radiopharmaceuticals: addendum 3 to ICRP Publication 53. ICRP Publication 106. Approved by the Commission in October 2007. *Ann ICRP.* 2008;38: 1–197.